

Adaptive cancellation of mains power interference in continuous gravitational wave searches with a hidden Markov model

Author 1, Author 2, etc. Kimpson, Suvorova, Liu, Melatos, Middleton, Evans, Moran, Meyers, any others?

(Dated: September 22, 2023)

Continuous gravitational wave searches with terrestrial, long-baseline interferometers are hampered by long-lived, narrowband features in the power spectral density of the detector noise, known as lines. Candidate GW signals which overlap spectrally with known lines are typically vetoed. Here we demonstrate a line subtraction method based on adaptive noise cancellation, using a recursive least squares algorithm, a common approach in electrical engineering applications, such as processing audio and biomedical signals. We validate the line subtraction method by combining it with a hidden Markov model, a standard continuous wave search tool, to detect a synthetic continuous wave signal with an unknown and randomly wandering frequency which overlaps with the strong mains power line at 60 Hz in the Laser Interferometer Gravitational Wave Observatory. **TK: 2-3 sentences of main results to go here.**

DOI:

I. INTRODUCTION

Instrumental noise artifacts in gravitational wave (GW) searches with terrestrial, long-baseline interferometers are classified according to their duration and spectral properties. Short-lived, non-stationary, recurrent noise events such as optomechanical glitches typically last for seconds and exhibit distinctive spectral signatures, e.g. they can be chirp-like [1–5]. Long-lived, quasi-stationary, broadband noise sources include seismic disturbances at low frequencies, test mass thermal fluctuations at intermediate frequencies, and photon shot noise at high frequencies [6–10]. Long-lived narrowband spectral artifacts — termed instrumental lines — are caused by electrical subsystems (e.g. mains power, clocks, oscillators), mechanical subsystems (e.g. test mass and beam-splitter violin modes) and calibration processes [11], although sometimes the origin of a specific feature is unknown. Instrumental lines are disruptive, especially for continuous wave (CW) searches where the target astrophysical signal is quasi-monochromatic and resembles the noise artifact spectrally. Many above-threshold candidates discovered in published CW searches are vetoed because they coincide with known instrumental lines [12–14], for instance, in data from Observing Run 3 (O3) with the Laser Interferometer Gravitational Wave Observatory (LIGO), Virgo and the Kamioka Gravitational Wave Detector (KAGRA) [e.g. 15–17]

Several techniques have been implemented by the LIGO-Virgo-KAGRA (LVK) Collaboration to identify, characterize and suppress instrumental noise artifacts [18, 19]. Some techniques identify and veto an artifact (or gate data segments) based on its time-frequency signature [20–22]. Other techniques perform offline noise subtraction with reference to auxiliary data from physical environmental monitors (PEMs) [23–26]. PEMs can be used to witness correlated noise and generate a reference signal directly or elucidate and quantify

multichannel couplings [27, 28]. Additionally some techniques are based on machine learning [29–32]. In CW searches specifically, the distinctive amplitude and frequency (Doppler) modulations associated with the Earth’s rotation and revolution respectively can be exploited to discriminate between terrestrial noise artifacts and astrophysical signals [33, 34].

In most of the situations above, the practical effect of an instrumental line is to excise the relevant part of the observing band from a CW search. That is, if an above threshold CW search candidate coincides with a known instrumental line, the candidate is vetoed under current practice without further analysis, such as comparing the expected strength of the noise line with the measured strength of the candidate¹. In this paper we take a first step towards lifting the above limitation. We introduce an adaptive noise cancellation (ANC) scheme based on an adaptive recursive least squares (ARLS) method which suppresses narrowband noise proportional to a known PEM reference signal. We then apply the ANC scheme to a CW search algorithm based on a hidden Markov model (HMM) which detects and tracks quasi-monochromatic GW signals with wandering frequency and has been tested and validated thoroughly in multiple LVK searches [12–14, 35]. We demonstrate with synthetic data that the ANC scheme and HMM algorithm together can successfully detect a GW signal lying under the 60 Hz mains power line, if the signal exceeds a well-defined minimum amplitude. The approach extends naturally to other instrumental lines, a topic for future work.

The paper is organized as follows. In Section II we outline a mathematical model for the 60 Hz mains power line

¹ A regularly updated log of narrowband instrumental lines in the LVK detector is maintained at dcc.ligo.org/LIGO-T2100200/public for public reference.

and the PEM reference signal, and justify the assumptions of the model by reference to data from the LIGO Livingston interferometer. In Section III we introduce ANC formulated as an ARLS method. In Section IV we deploy the ANC scheme in conjunction with an HMM Viterbi algorithm applied to synthetic GW strain data and demonstrate the successful recovery of a frequency-wandering CW signal. **TK: last sentence to be rewritten with a few extra sentences to describe what we actually do in final sections.**

II. POWER GRID INTERFERENCE

The goal of this paper is to detect a quasi-monochromatic GW signal in a data stream contaminated by two kinds of noise: additive Gaussian noise which is fundamental and irreducible, and additive non-Gaussian interference from a long-lived narrow spectral feature which can be filtered out in principle given an accurately measured reference signal. For this work we consider the spectral line at 60 Hz that results from the North American alternating current power grid as the additive non-Gaussian interference, as it is a long-standing impediment to many CW searches with the LIGO interferometers. In Section II A we briefly review the 60 Hz LIGO interference line before proceeding in Section II B to specify the assumed mathematical forms of the interference and reference signals. In Section II C we justify the assumptions of Section II B by analysing differential arm length (DARM channel) and environmental (power grid monitoring) data from the LIGO interferometers.

A. LIGO 60 Hz Interference

LIGO data contains multiple long-duration narrow lines in addition to the usual Gaussian noise. These lines are shown in Figure 1 where we plot the amplitude spectral density of the GW strain channel *:DCS-CALIB_STRAIN_C01_AR for both LIGO-Hanford (orange curve) and LIGO-Livingston (blue curve). The small amplitude random fluctuations are the result of Gaussian noise whereas the large amplitude spikes are the long-duration lines. The provision of mains power electricity in North America via an alternating current with frequency 60 Hz leads to a line in the power spectral density of the LIGO noise. The mains power couples to the GW strain channel, because the performance of the high-sensitivity electronic components within LIGO varies with respect to the input power voltage. Additionally, the magnetic fields that arise from the AC mains supply couple to magnets on optical components.

Some spectral lines are static, but the 60 Hz line wanders in time, due to variations in the load in the North American power grid. The wandering is displayed in the cascade plot in Figure 2, where the amplitude spectral

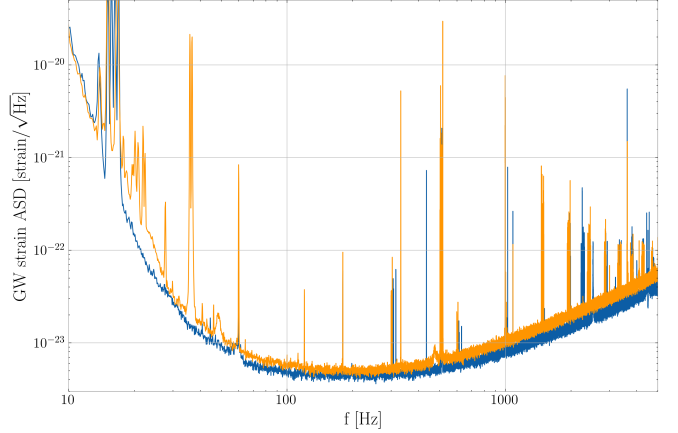


FIG. 1. Sensitivity plot for LIGO-Hanford (orange) and LIGO-Livingston (blue) for a snapshot of data (10.0 minutes) from O3 (channel *:DCS-CALIB_STRAIN_C01_AR, see Ref. [36, 37]). The vertical axis plots the amplitude spectral density of the detector noise in units of $\text{Hz}^{-1/2}$, while the horizontal axis plots the observation frequency in units of Hz. The spectral line at 60 Hz is clearly visible as a spike rising three decades, along with multiple other instrumental lines at other frequencies.

density of the output signal of the LIGO-Hanford PEM channel H1:PEM-CS_MAINSMON_EBAY_1_DQis plotted for 210 5-min samples stacked vertically. The peak of the amplitude spectral density varies from 59.969 Hz to 60.053 Hz, across the 210 samples with an average value of 60.004 Hz. Its full width half maximum varies from 5.294 mHz to 29.377 mHz, with an average value of 10.749 mHz. For a full review of LIGO spectral artifacts, including the 60 Hz line, we refer the reader to [11].

The 60 Hz line occurs in the neighbourhood of plausible astrophysical signals. For example, mass quadrupole radiation from a rotating mountain on the Crab pulsar would be emitted at twice the star's spin frequency, viz. 30.2 Hz [14] [13].

B. Statement of the problem: signal and noise models

Let $x(t)$ denote the scalar time series output by the GW strain channel of a LIGO-like long baseline interferometer. Suppose that $x(t)$ is sampled at discrete times t_n , with $1 \leq n \leq N$ and uniform sampling interval $\Delta t = t_n - t_{n-1}$. Let $r(t)$ denote the scalar time series output by the environmental reference channel relevant for filtering interference; here $r(t)$ is of one of the three phases of mains power measured at some reference point in the detector. The reference signal is usually sampled less frequently than $x(t)$ at discrete times t_{nk} , with $1 \leq k \leq K$ and $1 \leq n_k \leq N$. We assume for the sake of convenience that every t_{nk} coincides with some t_n for all

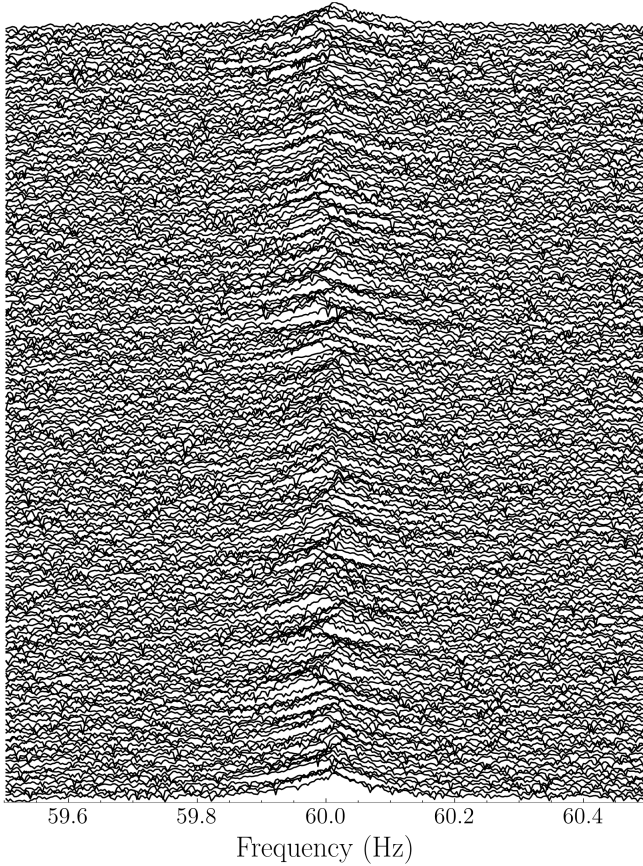


FIG. 2. Cascade plot showing the temporal evolution of the amplitude spectral density (units: $\text{Hz}^{-1/2}$) of the LIGO-Hanford mains-power PEM monitor H1:PEM-CS_MAINSMON_EBAY_1_DQ (corner station, phase 1) as a function of frequency (units: Hz). Each trace corresponds to 320 s (≈ 5 min) of data (210 traces stacked vertically). The peak of the mains power 60 Hz line wanders by $\approx \pm 30$ mHz about its time-averaged frequency.

k , but the condition is not essential.

The strain channel is composed of a gravitational wave signal $h(t)$, non-Gaussian interference $c(t)$ (sometimes called “clutter”) and Gaussian noise $n(t)$ in a linear combination,

$$x(t) = h(t) + c(t) + n(t) . \quad (1)$$

In this paper the gravitational wave signal takes the form predicted by Jaradowski *et al.* [38] for a biaxial rotor, e.g. a neutron star (NS) emitting gravitational waves at multiples of the star’s spin frequency f_* . The GW signal is quasi-monochromatic, amplitude-modulated by the rotation of the Earth and frequency-modulated by the Earth’s orbital motion. The noise $n(t)$ is white with $\langle n(t_n)n(t_{n'}) \rangle = \sigma_n^2 \delta_{nn'}$. Noise samples $n(t_n)$ are drawn from a Gaussian distribution with zero mean and variance σ_n^2 . The interference $c(t)$ takes a form determined by instrumental processes but is generally a

long-lived, narrowband spectral feature. We relate $c(t)$ to the mains voltage $r(t)$ in this paper.

Mains power is characterized by three properties. First, the frequency is maintained at a constant value across the grid to a good approximation by internal grid mechanisms (effectively a phase locked loop), with central frequency $f_{\text{ac}} = 60$ Hz in North America. A slow periodic modulation occurs around f_{ac} with a small amplitude $\Delta f_{\text{ac}} \lesssim 0.5$ Hz and period P , which wanders randomly and uniformly in the range $0 \leq P \leq P_{\text{max}}$. Second, the phase offset $\Theta(t)$ of the voltage $r(t)$ wanders stochastically. We assume that the phase noise is white and Gaussian, with $n_{\Theta}(t_n)$ drawn from a Gaussian distribution with zero mean and variance σ_{Θ}^2 , and $\langle n_{\Theta}(t_n)n_{\Theta}(t_{n'}) \rangle = \sigma_{\Theta}^2 \delta_{nn'}$. Third, the voltage amplitude, $A_r(t)$, is random. We assume that samples $A_r(t)$ are distributed uniformly within $[A_{\text{ac}} - \Delta A_{\text{ac}}, A_{\text{ac}} + \Delta A_{\text{ac}}]$. We can then write the reference voltage as,

$$r(t) = A_r(t_n) \cos [2\pi f_{\text{ac}} t + \Theta(t)] + n_r(t_n) , \quad (2)$$

with

$$\Theta(t) = 2\pi \Delta f_{\text{ac}} \cos \left[\frac{2\pi t}{P(t_n)} \right] + n_{\Theta}(t_n) , \quad (3)$$

for $t_n \leq t \leq t_{n+1}$. That is, at time t_n , random variables $A_r(t_n)$, $P(t_n)$ and $n_{\Theta}(t_n)$ are drawn from the distribution $\mathcal{U}[A_{\text{ac}} - \Delta A_{\text{ac}}, A_{\text{ac}} + \Delta A_{\text{ac}}]$, $\mathcal{U}[0, P_{\text{max}}]$, and $\mathcal{N}[0, \sigma_{\Theta}^2]$ respectively. Equation (2) then steps forward over a time interval Δt ; that is, $r(t)$ is discontinuous from one time step to the next due to random sampling. In Equation (2), $n_r(t_n)$ is the reference signal measurement noise at t_n , assumed to be white and Gaussian with $r_r(t_n)$ drawn from a Gaussian with zero mean and variance σ_r^2 . All the white measurement and process noises are assumed to be independent.

Mains power couples into the strain channel in various complicated ways, e.g. through electronic devices, or inductively through ambient magnetic fields. A central assumption in this work is that the interference in the strain channel is an exact, amplitude-scaled replica of the reference signal up to a delay τ_{delay} which is attributed to spatial propagation between the PEM site and the GW-sensing apparatus. Hence we can express the interference as,

$$c(t) = A_c(t_n - \tau_{\text{delay}}) \cos [2\pi f_{\text{ac}}(t_n - \tau_{\text{delay}}) + \Theta(t_n - \tau_{\text{delay}})] , \quad (4)$$

for $t_n \leq t \leq t_{n+1}$. The amplitude A_c is distributed as $\mathcal{U}[A_{\text{ac}} - \Delta A_{\text{ac}}, A_{\text{ac}} + \Delta A_{\text{ac}}]$. For this work we consider $0 \leq \tau_{\text{delay}} \leq 10\Delta t$, but wider or narrower ranges are possible and straightforward to implement. The assumption that $c(t)$ is a scaled replica of $r(t)$ is tested in Section II C.

C. Cross-correlating $x(t)$ and $r(t)$

A key assumption in Section II B is that the 60 Hz interference recorded in the reference PEM channel is

also present in the strain channel. That is, the mains voltage recorded by the PEM is imprinted onto the strain channel up to a proportionality constant and time delay. In order to test this assumption we cross-correlate the strain channel and the PEM channel.

We use open source data for the strain and PEM channels from the first part of the third LIGO observing run, O3a [36]. These data are obtained via the Gravitational Wave Open Science Center ² using the GWPY package [39]. In the auxiliary O3a data there are nine PEM channels at LIGO-Livingston and seven PEM channels at LIGO-Hanford ³. In this paper we consider just the LIGO-Livingston data, as they suffice to make the point.. The strain data are sampled at 16384 Hz and downsampled to 4096 Hz to match the sampling rate of the PEM channels.

Figure II C displays the coherence

$$C_{xy} = ABC \quad (5)$$

between each of the 9 PEM channels and the high latency, calibrated strain channel L1:DCS-CALIB_STRAIN_C01_AR over a 10 minute interval. For all channels there is a clear spike feature at 60 Hz. The coherence feature has an amplitude ≥ 0.5 UNITS for seven of the nine PEM channels. C_{xy} is weakest for the channels L1:PEM-EY_MIC_VEA_PLUSY_DQ and L1:PEM-CS_MIC_LVEA_INPUTOPTICS_DQ. These channels corresponds to microphone PEMs in the LIGO vacuum equipment area and are less sensitive to the 60 Hz noise than e.g. L1:PEM-EY_MAINSMON_EBAY_1_DQ which directly measures the mains voltage of the power supply to the LIGO central building

TK: what is the point of this figure? What are we trying to show? Figure 4 displays the coherence spectrogram, i.e. the time-varying coherence between the strain channel and the PEM channel L1:PEM-CS_MAINSMON_EBAY_1_DQ. C_{xy} is calculated in 10-s blocks; that is, every pixel in Figure 4 is 10 s wide horizontally. We observe similar results to Figure II C. There is a strong spectral feature at 60 Hz which persists for the full 10 min covered by Figure 4. Additional features are seen near 0.2 kHz and 0.3 kHz, corresponding to instrumental lines recorded by the PEM which imprint onto the strain channel and are unrelated to the mains power. Figures II C and 4 justify in part the assumptions in Section II B.

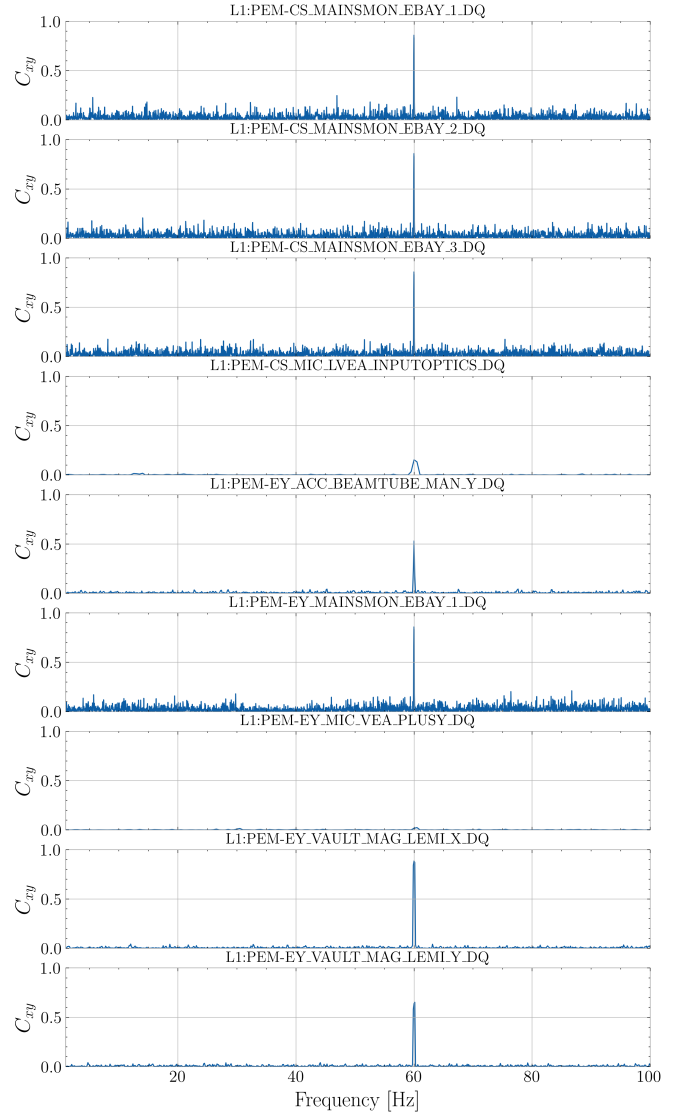


FIG. 3. Coherence C_{xy} defined by Equation 5 between the LIGO-Livingston strain channel L1:DCS-CALIB_STRAIN_C01_AR and the nine mains-power PEM channels during a 10 minute observation. Clear features at 60 Hz are present in every channel. C_{xy} is lowest in the fourth and seventh panels, which correspond to microphones in the vacuum equipment area, which do not measure the mains voltage directly.

III. ADAPTIVE NOISE CANCELLATION

Adaptive Noise Cancellation (ANC) is a method for recovering an estimate of an underlying signal which has been corrupted or obscured by some additive noise interference [40]. In contrast to other common optimal filtering methods (e.g. Wiener, Kalman) ANC requires no a-priori knowledge of either the signal or the noise. Instead, ANC makes use of a reference input which is correlated in some unknown way to the noise in the

² <https://gwosc.org/>

³ <https://git.ligo.org/gwosc/tutorials/gwosc-aux-tutorials/-/tree/main/Channels>

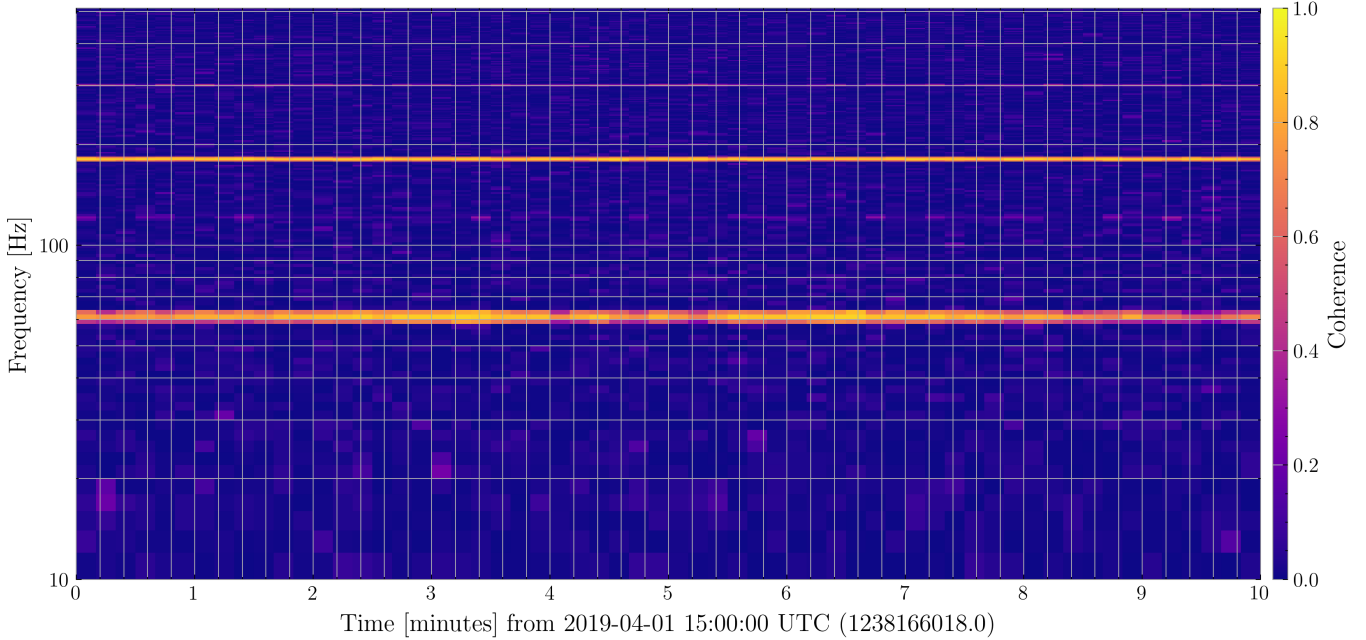


FIG. 4. Coherence spectrogram between the strain channel L1:DCS-CALIB_STRAIN_C01_AR and the PEM channel L1:PEM-CS_MAINSMON_EBAY_1_DQ over a 10 minute period of O3 data. A strong coherence is observed at 60 Hz due to the main power interference. Additional coherence can also be observed at ~ 200 Hz and 300 Hz due to instrumental lines of a different provenance c.f. Fig 1.

primary signal. This reference can then be filtered and subtracted from the primary data series so as to recover the underlying signal. For our purposes, the primary timeseries is the gravitational-wave strain channel $x(t)$ (Equation (1)) and the reference is a PEM recording voltage data from the power grid $r(t)$ (Equation (2)). The objective of ANC is then to remove the clutter $c(t)$ of Equation (1) with the aid of $r(t)$ whilst leaving $h(t)$ i.e. the signal of interest, intact. We now describe the ANC implementation used in this work.

The reference $r(t)$ is used to construct an estimate of the clutter, $\hat{c}(t)$. The clutter estimate can then be subtracted from the primary signal in the time domain, defining a residual $e(t)$:

$$e(t) = x(t) - \hat{c}(t) . \quad (6)$$

As $\hat{c}(t) \rightarrow c(t)$, $e(t) \rightarrow h(t) + n(t)$ and we recover a noise cancelled timeseries. The clutter estimate is modelled by a finite duration impulse response (FIR) filter:

$$\hat{c}_k = \mathbf{w}^\top \mathbf{u}_k . \quad (7)$$

where \hat{c}_k is the clutter estimate at a discrete timestep k (i.e. $\hat{c}_k = \hat{c}(t_{n_k})$), \mathbf{u}_k is the tap-input vector composed of M running samples of the reference signal arranged backwards in time:

$$\mathbf{u}_k = [r_k, r_{k-1}, \dots, r_{k-M+1}] , \quad (8)$$

and \mathbf{w} is the tap-weight vector:

$$\mathbf{w} = [w_1, w_2, \dots, w_M] . \quad (9)$$

We want to determine the optimal tap weights \mathbf{w}_{opt} , those which minimise the mean square error cost function:

$$\mathbf{w}_{\text{opt}} = \arg \min_{t=t_1}^{t=t_N} |e(t)|^2 . \quad (10)$$

This minimization problem can be solved by way of an adaptive recursive least squares (ARLS) method which we now describe in Section III A

A. Adaptive Recursive Least Squares Method

We now outline the ARLS method to compute the optimal tap weights and estimate the noise-subtracted signal.

1. Initialise the tap weights $\mathbf{w} = \mathbf{0}$ and a covariance matrix $\mathbf{P} = \delta^{-1} \mathbf{I}$, for regularisation parameter $0 < \delta \ll 1$ and identity matrix \mathbf{I} of rank M .
2. For $k = 1, \dots, K$:
 - (a) Estimate the clutter \hat{c}_k by Equation 7
 - (b) Calculate the residual e_k by Equation 6

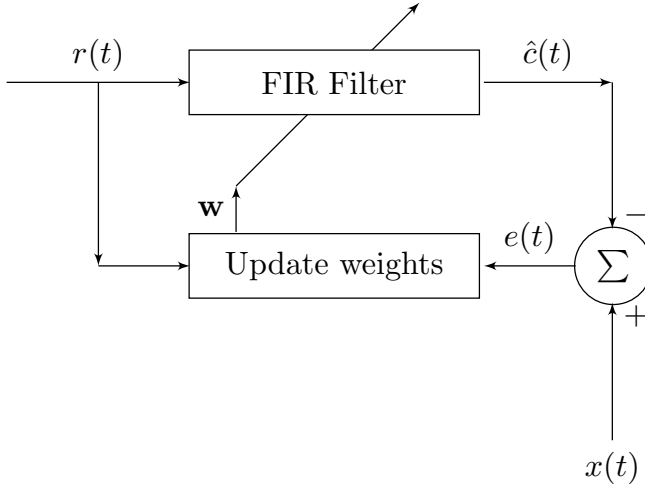


FIG. 5. Block diagram of the adaptive recursive least squares method described in Section III A. The reference signal $r(t)$ is passed to an FIR filter to construct an estimate of the signal clutter $\hat{c}(t)$. Subtracting the clutter estimate from the primary signal $x(t)$ provides a residual $e(t)$ which can then be used to update the weights \mathbf{w} of the FIR filter and the method proceeds iteratively.

(c) Calculate the gain vector

$$\mathbf{g}_k = \frac{\mathbf{P}\mathbf{u}_k}{\lambda + \mathbf{u}_k^T \mathbf{P} \mathbf{u}_k} \quad (11)$$

(d) Update the tap weights

$$\mathbf{w} += e_k \mathbf{g} \quad (12)$$

(e) Update the covariance matrix

$$\mathbf{P} += \lambda^{-1} \mathbf{P} - \mathbf{g} \lambda^{-1} \mathbf{P} \mathbf{u}_k^T \quad (13)$$

The algorithm is also illustrated in Figure 5 via a block diagram.

ARLS has two free parameters: the order parameter M and the “forgetting factor” λ , which is chosen so as to give exponentially less weight to older samples. The choice of M influences the latency of the FIR filter, the computational overhead and the filter accuracy. In Sec. IV we trial a selection of M values for synthetic GW data. The forgetting factor λ ranges between 0 and 1, with $\lambda = 1$ corresponding to infinite memory, causing the filter becomes an ordinary least squares method. In this work we use $\lambda = 0.9999$. We refer the reader to Chapter 9 of Ref. [41] for a full review of adaptive least squares estimation in the context of linear filtering.

IV. HMM VALIDATION TESTS

We want to test the ANC method described in the preceding section by trying to search for a continuous wave

signal which has an initial frequency $f_{\text{GW}}(t=0) = 60\text{Hz}$, coincident with the instrumental line from the mains power grid. We search for the CW signal using a HMM scheme based on the Viterbi algorithm [42, 43]. Specifically, we use the method introduced by Suvorova *et al.* [35], which has been thoroughly tested through multiple LVK searches [12–14]. We do not cover any details of the HMM scheme in this work and refer the reader to Suvorova *et al.* [35] for further information. The GW signal is obscured in the data by the presence of the mains power instrumental line. The challenge is to try to recover the signal by first passing the data $x(t)$ through the ANC filter before using the HMM tracker on this filtered dataset to try to recover the signal. In Section IV A we describe how we create a synthetic dataset $x(t)$. In Section IV B we introduce a representative example, illustrating the frequency tracking before and after ANC. In Section IV C we explore the performance of the ANC filter in response to different characteristics of the interference signal, e.g. variations in the central frequency f_{ac} relative to the initial GW frequency. In Section IV D we investigate the performance of the filter in response to different filter settings; the order of the filter M (i.e. the number of taps) and the number of reference channel inputs.

A. Creating simulated data

Throughout this paper we work with some representative synthetic data, $x(t)$, rather than directly with the LIGO data itself. We can construct synthetic data for each of the constituent parts of Equation (1) - the GW signal of interest, the Gaussian noise and the noise clutter via the formulation described in Section II B as follows.

The GW frequency evolves in general due to the intrinsic evolution of the due to the intrinsic evolution of the source. For this paper we assume that the source is isolated (i.e. it is not in a binary) and that the GW is monochromatic (i.e. all temporal derivatives of the frequency are zero). We also consider the GW source to be at a constant location with respect to the observer and neglect all contributions due to e.g. the rotation and revolution of the Earth. Under these assumptions the GW model reduces to

$$h(t) = h \sin(2\pi\phi_{\text{GW}}(t)) , \quad (14)$$

where h is the constant GW amplitude and $\phi(t)$ a random phase variable which is the integral of the underlying, piecewise linear GW frequency f_{gw} i.e.

$$\phi_{\text{GW}}(t) = \int_0^t f_{\text{gw}}(s) ds . \quad (15)$$

The GW frequency at discrete timestep m within the sampling interval Δt is labelled as $f_{\text{gw}}^{(m)}$ and evolves ac-

cording to

$$f_{\text{gw}}^{(m+1)} = f_{\text{gw}}^{(m)} + \delta_m \Delta t , \quad (16)$$

with δ_m a zero mean Gaussian noise at timestep m , with variance σ_f^2 ,

$$\delta_m = \mathcal{N}(0, \sigma_f^2) \quad (17)$$

The synthetic GW signal $h(t)$ is then completely described by the parameters h and σ_f^2 , and the initial GW frequency $f_{\text{gw}}(t=0)$

The clutter and reference signal evolve according to Equations (2) and (4) respectively. For this initial study we take the reference voltage to have a constant amplitude $A_r(t) = a_r$, the clutter to have a corresponding constant amplitude $A_c(t) = a_c$. We also assume that the modulation in the reference voltage about f_{ac} has a constant amplitude Δf_{ac} with a constant period $P(t) = P$. Throughout this work we take $\Delta f_{\text{ac}} = 1/2\pi$ Hz⁴. We define the variable $\gamma = P^{-1}$ and explore different values for γ in Section IV C. Under these assumptions, Equations (2) and (4) reduce to

$$r(t) = a_r \cos [2\pi f_{\text{ac}} t + 2\pi \cos(2\pi\gamma t) + n_\Theta(t)] + n_r(t) , \quad (18)$$

$$c(t) = a_c \cos [2\pi f_{\text{ac}} t' + 2\pi \cos(2\pi\gamma t') + n_\Theta(t')] . \quad (19)$$

The synthetic reference and clutter data are then completely described by the amplitude parameters a_r, a_c , the central frequency f_{ac} , the timescale γ and the noise covariances $\sigma_\Theta^2, \sigma_r^2$. For convenience we reparametrise f_{ac} relative to the initial GW frequency at $t = 0$, defining the new variable

$$\Delta f = |f_{\text{ac}} - f_{\text{gw}}(t=0)| \quad (20)$$

The 9 free parameters of the model are summarised in Table I. We have 3 amplitude parameters h, a_r, a_c for the GW, reference and clutter respectively, with $h \ll a_c, a_r$. There are 4 noise parameters $\sigma_n, \sigma_\Theta, \sigma_r, \sigma_f$ for the Gaussian noise $n(t)$, the voltage phase noise $n_\Theta(t)$, reference signal measurement noise $n_r(t)$ and the GW frequency noise Equation 17 respectively. Additionally we have the absolute difference between the central frequency and the initial GW frequency, Δf and the timescale of the modulation in the central frequency, γ .

Throughout this work when creating synthetic data, f_{ac} is fixed at 60 Hz. The terrestrial noise parameters, $\sigma_n^2, \sigma_r^2, \sigma_\Theta^2$ are also fixed. TK: other summary text on choice of parameters for synthetic data to go here. Waiting on input from Sofia on which parameters were actually used for the data

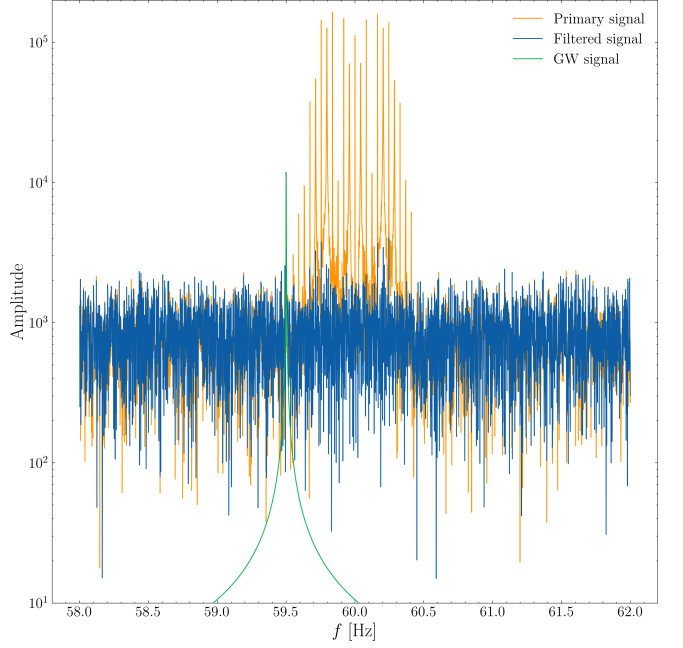


FIG. 6. Fourier response of the data $x(t)$ (orange), the GW signal $h(t)$ (green) and the ANC filtered data $x(t) - \hat{e}(t)$ (blue) for a system with parameters described in Table I. ANC filters out the excess power that results from the interference signal about the central 60 Hz frequency.

B. Representative example

In order to demonstrate the effectiveness of ANC in conjunction with an HMM Viterbi search in this section we consider two representative examples where $h = 0.025$ and the stochastic GW frequency wandering is either ‘low’, $\sigma_f^2 = 0.01$ Hz $s^{-1/2}$ or ‘high’, $\sigma_f^2 = 0.1$ Hz $s^{-1/2}$. All other free parameters of the model are as specified in Table I. At this stage we assume that we have just one single reference PEM channel.

Initially we verify that the ANC filter works as expected to remove the excess power from the 60 Hz

Parameter	Physical meaning	Injected Value
h	Strain amplitude	-
a_r	Voltage amplitude	-
a_c	Clutter amplitude	-
σ_n^2	Gaussian noise covariance	-
σ_r^2	Voltage measurement noise	-
σ_Θ^2	Voltage phase noise	-
σ_f^2	GW frequency noise	-
Δf	Central frequency shift	-
γ	Modulation frequency	-

TABLE I. Summary of parameters used to create synthetic data for testing the ANC method in Section IV, their physical meaning, and the injected values used throughout this work.

⁴ TK: I have guessed that this is what is happening under the hood of the code, but need to verify with Sofia/Changrong.

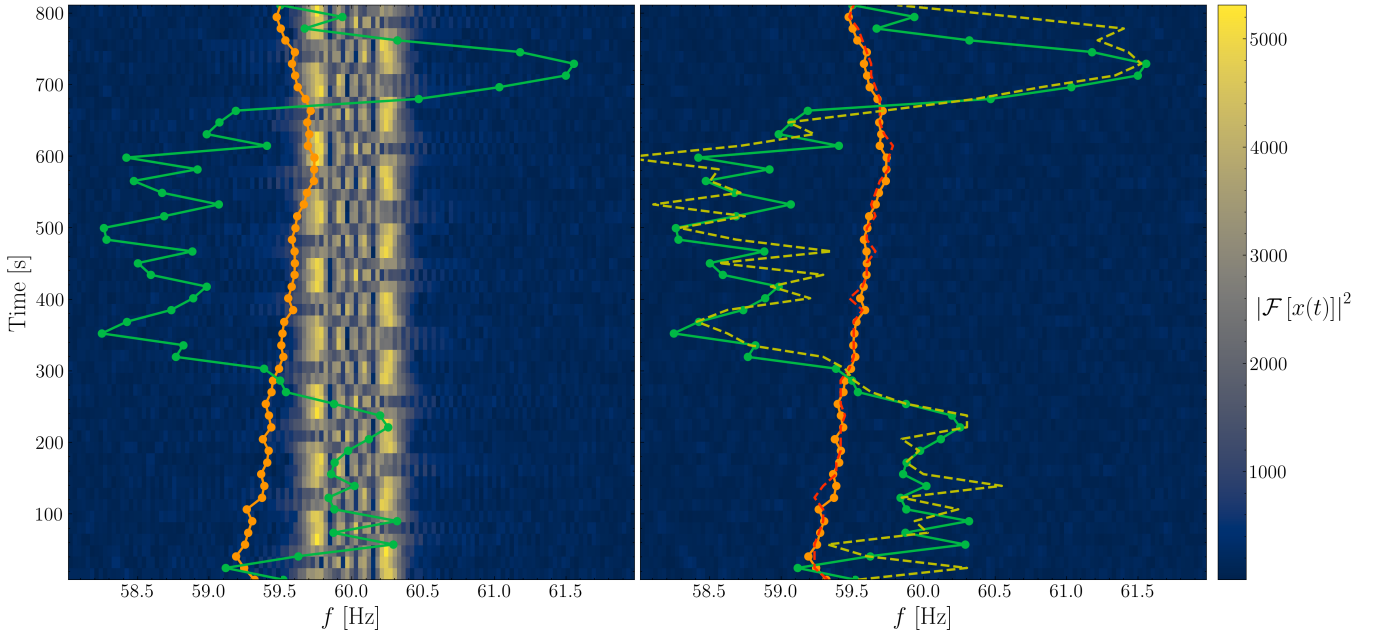


FIG. 7. Fourier amplitude spectrogram and tracking of the frequency evolution of a continuous GW with $h = 0.025$ and $\sigma_f^2 = \{0.01, 0.1\} \text{ Hz s}^{-1/2}$ (orange and green lines respectively) using a HMM Viterbi algorithm. *Left panel:* before applying ANC filtering to remove the interference signal centred at 60 Hz, *Right panel:* after applying ANC. The Viterbi estimates of the spin wandering are noted by the dashed coloured lines. Before ANC, the Viterbi algorithm is unable to track the spin wandering. After ANC the Viterbi algorithm is able to track the GW frequency accurately for both the high and low noise cases.

interference. In Figure 6 we show the Fourier amplitude of the synthetic data $x(t)$, the underlying GW signal $h(t)$, and the signal after being passed through the ANC filter, $e(t) = x(t) - \hat{c}(t)$ across the frequency range 58 - 62 Hz, for the case where $\sigma_f^2 = 0.01 \text{ Hz}$. Before filtering the Fourier spectrum of $x(t)$ has multiple modes about the central 60 Hz frequency as a result of the interference clutter. This clutter obscures the power from the GW signal. After filtering, this excess power is removed and the Fourier spectrum of $e(t)$ is flat, with the exception of a clear feature coincident with the central frequency of the injected GW.

Having established the ability of the ANC method to filter out the interference clutter given a reference signal, we can deploy the ANC in conjunction with the Viterbi HMM. We pass the ANC filtered data to the HMM and evaluate the performance of the HMM in tracking the spin-wandering continuous wave signal. The results are shown in Figure 7 for the case of both low and high frequency wandering, for a single realisation of the noise. The figure shows the Fourier amplitude spectrogram of the data $x(t)$ before and after the application of ANC filtering. The spin wandering of the GW source (green/orange lines) and the Viterbi estimate (dashed orange/yellow lines) of the spin wandering is superimposed onto the spectrogram. In the low noise case the GW spin frequency wanders close to, but below, the 60 Hz

interference line. In the high noise case the GW spin frequency wanders much more strongly over a larger range of frequencies and crosses the interference line, presenting a more difficult challenge for the Viterbi tracking algorithm. Before ANC there is a clear feature in the Fourier spectrogram corresponding to the 60 Hz interference signal. In this case the Viterbi algorithm is unable to track the GW spin wandering frequency signal which is submerged with respect to the voltage interference at 60 Hz. Conversely, the application of the ANC enables the interference to be removed without perturbing the gravitational wave signal. In this case the Viterbi algorithm is able to track the GW frequency wandering in both the low and high noise cases with high fidelity. Specifically, the mean squared error in the frequency estimate is $1.4 \times 10^{-3} \text{ Hz}$ for the low noise case and 0.22 Hz for the high noise case.

C. ROC curves versus power line parameters

With the performance of the ANC and Viterbi approach established for a single example, it is of interest to explore how the algorithm performs for different power line parameters. In this section we vary Δf and γ to test how the combined ANC filter and Viterbi algorithm perform across multiple noise realisations. To this end we calculate the detection probability compared

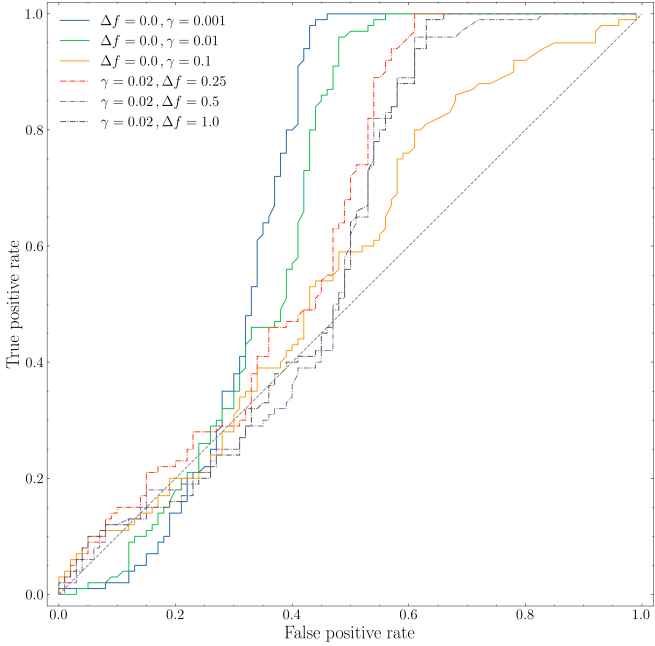


FIG. 8. ROC curve over multiple noise realisations for different power line parameters. All other parameters are as specified in Table I. There is an evident high false alarm rate for all parameters, with a low AUC value of 0.55 for $\Delta f = 0.0, \gamma = 0.1$, and a high AUC value of 0.68 for $\Delta f = 0.0, \gamma = 0.001$. The high false alarm rate is a result of the interference not being completely removed by the ANC filter.

to the false alarm probability, i.e. the receiver operating characteristic (ROC), for the Viterbi search after the data has been filtered using ANC. We consider two situations. In the first situation we hold Δf constant at $\Delta f = 0.0$ and set $\gamma = \{0.001, 0.01, 0.1\}$. In the second situation we hold γ constant at $\gamma = 0.02$ and set $\Delta f = \{0.25, 0.5, 1.0\}$. The results are shown in Figure 8. Whilst the underlying wandering GW frequency signal can generally be tracked well for a single noise realisation (c.f. Figure 7), we can see that for these power line parameters, across multiple noise realisations there is a high false alarm rate. This is a consequence of the interference not being completely removed and evidences how even a small quantity of clutter noise is sufficient to corrupt the search for continuous waves. To quantify the performance with a single scalar value we consider the Area Under the Curve (AUC), a common metric used to evaluate ROC curves. The AUC can be in the range $0.5 - 1.0$, where $AUC = 0.5$ corresponds to the performance of a random classifier (i.e. the grey dashed diagonal line in the figure) and $AUC = 1.0$ represents a perfect classifier. For the first situation with $\Delta f = 0.0$ and $\gamma = \{0.001, 0.01, 0.1\}$, $AUC = \{0.68, 0.65, 0.55\}$ respectively. For the second situation with $\gamma = 0.02$ and $\Delta f = \{0.25, 0.5, 1.0\}$, $AUC = \{0.62, 0.58, 0.58\}$ respectively. Whilst the method performs better than a random classifier for all parameters, the AUC values are generally

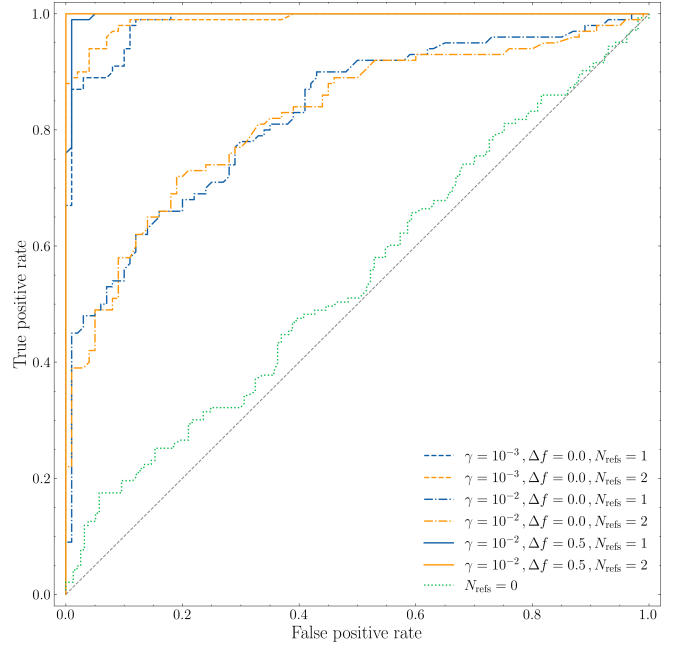


FIG. 9. ROC curve for 3 different systems: System A with $\{\gamma = 0.001, \Delta f = 0.0\}$, System B with $\{\gamma = 0.01, \Delta f = 0.0\}$ and System C with $\{\gamma = 0.01, \Delta f = 0.5\}$ (dotted, dashed, solid lines respectively). The orange lines denote the Viterbi search run with 2 reference channels, the blue lines using 1 reference channel. The green dotted line is the detection performance in the absence of ANC filtering. The grey dashed line is the performance of a random classifier. Detection using ANC filtering consistently outperforms that without ANC filtering. ANC filtering using 2 reference channels generally outperforms that using a single reference channel.

N_{refs}	System		
	A	B	C
1	0.975	0.827	0.987
2	0.990	0.822	0.999

TABLE II. Summary of AUC values for each of the ROC curves presented in Figure 9. Adding an extra PEM reference generally improves the detection performance, with the exception of system B. The AUC value for the zero PEM reference case (i.e. no ANC filtering) is $AUC = 0.55$.

low, especially for cases where the interference has a large amplitude with a long period. In Section IV D we explore the use of different parameters used for the ANC filter, including the inclusion of additional reference channels

D. ROC curves vs. filter parameters

We have shown that the ANC filter used in conjunction with the Viterbi algorithm is effective at tracking the wandering GW spin frequency, but suffers from a high false alarm rate for the particular parameters of the

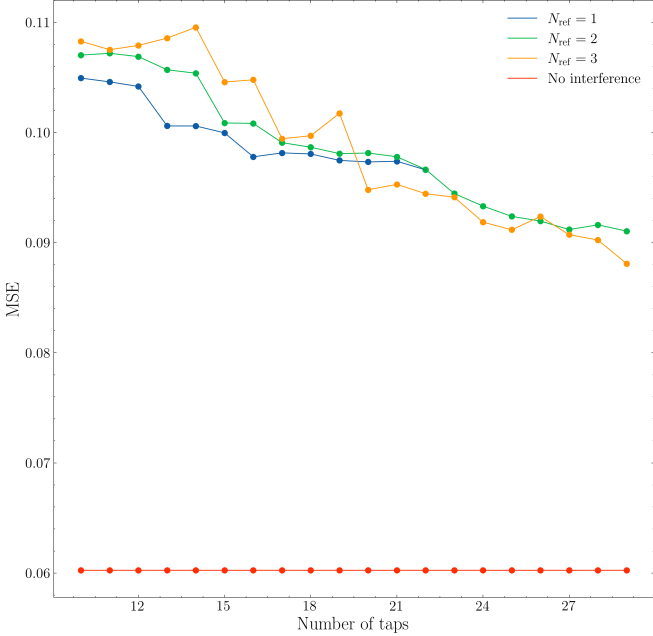


FIG. 10. Mean square error (MSE) in the Viterbi estimates of the GW wandering spin frequency for a system with $h = 0.025$ and $\Delta f = 0.0$ relative to the number of taps used in the FIR filter. Up to three PEM reference channels are used. The solution for the case with zero interference clutter is also shown.

ANC filter that we have been using. In this Section we investigate two important questions:

1. How does ANC benefit from multiple independent references?
2. What order ANC filter (M) is required to achieve good interference cancellation?

Regarding the first question, the preceding validation tests on synthetic data all assumed that we have a single PEM reference voltage measurement. However, as discussed in Section II C in practice there are multiple PEM channels measuring power line interference for LIGO (c.f. Figure II C). Specifically, in the open O3a data there are 9 PEM channels for LIGO-Livingston and 7 PEM channels for LIGO-Hanford. Multiple PEM channels provided additional independent measurements of the reference voltage; it seems reasonable to suspect that these additional channels may aid the performance of the ANC filter. Indeed, ANC is commonly used with multiple reference signals in other electrical engineering applications such as noise cancelling headphones [44], communication intelligibility [45, 46] and cardiac monitoring [47].

In Figure 9 we present the ROC curves for 3 different example systems:

- **System A.** $\gamma = 10^{-3}$, $\Delta f = 0.0$. Dashed lines in

the figure.

- **System B.** $\gamma = 10^{-2}$, $\Delta f = 0.0$. Dash-dotted in the figure
- **System C.** $\gamma = 10^{-2}$, $\Delta f = 0.5$. Solid lines in the figure

For each system we compute the ROC curve over multiple noise realisations for both one and two reference channels (blue, and orange lines respectively). This gives us six total ROC curve solutions. For comparison we also plot the case where we run the Viterbi search for one of the example systems, but with zero PEM references (dotted green line). The specific AUC values for each ROC curve are reported in Table II.

We can see that for all example systems the detection probability is high with respect to the false alarm probability. The detection probability using ANC filtering is greater than without ANC filtering for all systems (i.e. the orange and blue lines are exclusively above the green dotted line). Specifically the for the zero filtering case $AUC = 0.54$, whilst all cases which use ANC filtering have $AUC \geq 0.82$ and as high as $AUC = 0.99$. The inclusion of an additional reference channel improves the detection probability for Systems A and C, with the AUC values rising from 0.975 to 0.990 for System A and from 0.987 to 0.999 for System B. No improvement is observed for System B, with $AUC = 0.827$ for $N_{\text{ref}} = 1$ and $AUC = 0.822$ for $N_{\text{ref}} = 2$. The lack of improvement for System B when using two PEM references suggests that for these parameters a single reference is sufficient to capture the dynamics of the interference clutter.

⁵

Regarding the second question, the order of the filter, i.e. the number of taps, is a parameter that can be freely chosen in ARLS. It is important to consider the filter's robustness to the choice of M . Generally an increased number of taps is expected to improve the performance of the filter due to the increased model complexity. However, this comes at an increased computational cost and also an increased latency. For real time applications tracking the wandering of the GW frequency it is important to minimize both of these variables. In Figure 10 we plot the mean squared error (MSE) in the GW frequency estimated by Viterbi compared to the true spin-wandering frequency, averaged over multiple noise realisations. We set the system to have $h = 0.025$ and $\Delta f = 0.0$ and consider up to three PEM reference channels. As a reference we also plot the error in the Viterbi estimates for the case where there is no interference clutter and so no ANC is required. We can see that generally the accuracy improves with an increased number of taps. When M is small the

⁵ TK: Why are these results so different to Figure 8? Has the strain amplitude changed? Need to check with Sofia

$N_{\text{ref}} = 1$ solution generally outperforms the high N_{ref} solutions; in this regime the number of taps is sufficiently small to not be able to take advantage of the increased information provided by the additional reference channels. Conversely as the number of taps increases, the $N_{\text{ref}} = 3$ becomes the best performing solution. We note that rather than explicitly specifying the number of taps, adaptive tap length methods that automatically update the number of taps used are also available [e.g. 48–50].

V. CONCLUSIONS

In this paper we demonstrate a new line subtraction method based on adaptive noise cancellation for use in

continuous gravitational wave searches. We use an adaptive recursive least squares method in conjunction with an independent, known PEM reference signal to suppress the interference from a long-lived narrow spectral feature. We then search for the continuous wave signal using a HMM Viterbi algorithm. We test our method on synthetic data containing the 60 Hz spectral interference line due to the North American power grid. We show how the ANC and Viterbi algorithm together are able to successfully track the spin-wandering continuous GW signal near the 60 Hz line. We test the method over multiple noise realisations and show TK: to confirm. The performance of the filter is generally improved with an increased number of reference signals and at an increased model order.

-
- [1] L. Blackburn, L. Cadonati, S. Caride, S. Caudill, S. Chatterji, N. Christensen, J. Dalrymple, S. Desai, A. Di Credico, G. Ely, *et al.*, *Classical and Quantum Gravity* **25**, 184004 (2008), arXiv:0804.0800 [gr-qc].
- [2] J. Aasi, J. Abadie, B. P. Abbott, R. Abbott, T. D. Abbott, M. Abernathy, T. Accadia, F. Acernese, C. Adams, *et al.*, *Classical and Quantum Gravity* **29**, 155002 (2012), arXiv:1203.5613 [gr-qc].
- [3] J. Aasi, J. Abadie, B. P. Abbott, R. Abbott, T. Abbott, M. R. Abernathy, T. Accadia, F. Acernese, C. Adams, T. Adams, *et al.*, *Classical and Quantum Gravity* **32**, 115012 (2015), arXiv:1410.7764 [gr-qc].
- [4] B. P. Abbott, R. Abbott, T. D. Abbott, M. R. Abernathy, F. Acernese, K. Ackley, M. Adamo, C. Adams, T. Adams, P. Addesso, *et al.*, *Classical and Quantum Gravity* **33**, 134001 (2016), arXiv:1602.03844 [gr-qc].
- [5] J. Glanzer, S. Soni, J. Spoon, A. Effler, and G. González, arXiv e-prints , arXiv:2304.07477 (2023), arXiv:2304.07477 [astro-ph.IM].
- [6] LIGO Scientific Collaboration, J. Aasi, B. P. Abbott, R. Abbott, T. Abbott, M. R. Abernathy, K. Ackley, C. Adams, T. Adams, P. Addesso, and et al., *Classical and Quantum Gravity* **32**, 074001 (2015), arXiv:1411.4547 [gr-qc].
- [7] B. P. Abbott, R. Abbott, T. D. Abbott, S. Abraham, F. Acernese, K. Ackley, C. Adams, V. B. Adya, C. Affeldt, M. Agathos, *et al.*, *Classical and Quantum Gravity* **37**, 055002 (2020), arXiv:1908.11170 [gr-qc].
- [8] .
- [9] T. Akutsu, M. Ando, K. Arai, Y. Arai, S. Araki, A. Araya, N. Aritomi, H. Asada, Y. Aso, S. Bae, *et al.*, *Progress of Theoretical and Experimental Physics* **2021**, 05A102 (2021), arXiv:2009.09305 [gr-qc].
- [10] P. Nguyen, R. M. S. Schofield, A. Effler, C. Austin, V. Adya, M. Ball, S. Banagiri, K. Banowetz, C. Billman, C. D. Blair, *et al.*, *Classical and Quantum Gravity* **38**, 145001 (2021), arXiv:2101.09935 [astro-ph.IM].
- [11] P. B. Covas, A. Effler, E. Goetz, P. M. Meyers, A. Neunzert, M. Oliver, B. L. Pearlstone, V. J. Roma, R. M. S. Schofield, V. B. Adya, and et al., *Phys. Rev. D* **97**, 082002 (2018), arXiv:1801.07204 [astro-ph.IM].
- [12] O. J. Piccinni, *Galaxies* **10**, 72 (2022), arXiv:2202.01088 [gr-qc].
- [13] K. Riles, *Living Reviews in Relativity* **26**, 3 (2023), arXiv:2206.06447 [astro-ph.HE].
- [14] K. Wette, *Astroparticle Physics* **153**, 102880 (2023), arXiv:2305.07106 [gr-qc].
- [15] R. Abbott, H. Abe, F. Acernese, K. Ackley, N. Adhikari, R. X. Adhikari, V. K. Adkins, V. B. Adya, C. Affeldt, D. Agarwal, M. Agathos, K. Agatsuma, N. Aggarwal, O. D. Aguiar, *et al.* (LIGO Scientific Collaboration, Virgo Collaboration, and KAGRA Collaboration), *Phys. Rev. D* **106**, 062002 (2022).
- [16] R. Abbott, T. D. Abbott, S. Abraham, F. Acernese, K. Ackley, A. Adams, C. Adams, R. X. Adhikari, V. B. Adya, C. Affeldt, D. Agarwal, M. Agathos, K. Agatsuma, N. Aggarwal, O. D. Aguiar, *et al.*, *Astrophys. J.* **921**, 80 (2021), arXiv:2105.11641 [astro-ph.HE].
- [17] R. Abbott, T. D. Abbott, F. Acernese, K. Ackley, C. Adams, N. Adhikari, R. X. Adhikari, V. B. Adya, C. Affeldt, D. Agarwal, M. Agathos, K. Agatsuma, N. Aggarwal, O. D. Aguiar, L. Aiello, *et al.*, *Astrophys. J.* **932**, 133 (2022), arXiv:2112.10990 [gr-qc].
- [18] D. Davis, J. S. Areeda, B. K. Berger, R. Bruntz, A. Effler, R. C. Essick, R. P. Fisher, P. Godwin, E. Goetz, A. F. Helmling-Cornell, *et al.*, *Classical and Quantum Gravity* **38**, 135014 (2021), arXiv:2101.11673 [astro-ph.IM].
- [19] D. Davis and M. Walker, *Galaxies* **10** (2022), 10.3390/galaxies10010012.
- [20] B. P. Abbott, R. Abbott, T. D. Abbott, M. R. Abernathy, F. Acernese, K. Ackley, C. Adams, T. Adams, P. Addesso, R. X. Adhikari, *et al.*, *Classical and Quantum Gravity* **35**, 065010 (2018), arXiv:1710.02185 [gr-qc].
- [21] J. Lee, S. H. Oh, K. Kim, G. Cho, J. J. Oh, E. J. Son, and H. M. Lee, *Phys. Rev. D* **103**, 123023 (2021).
- [22] B. Steltner, M. A. Papa, and H.-B. Eggenstein, *Phys. Rev. D* **105**, 022005 (2022), arXiv:2105.09933 [gr-qc].
- [23] J. C. Driggers, M. Evans, K. Pepper, and R. Adhikari, *Review of Scientific Instruments* **83**, 024501 (2012), arXiv:1112.2224 [gr-qc].
- [24] V. Tiwari, M. Drago, V. Frolov, S. Klimenko, G. Mitselmakher, V. Necula, G. Prodi, V. Re, F. Salemi, G. Venedovato, and I. Yakushin, *Classical and Quantum Gravity* **32**, 165014 (2015), arXiv:1503.07476 [gr-qc].
- [25] D. Davis, T. Massinger, A. Lundgren, J. C. Driggers, A. L. Urban, and L. Nuttall, *Classical and Quan-*

- tum Gravity **36**, 055011 (2019), arXiv:1809.05348 [astro-ph.IM].
- [26] J. C. Driggers, S. Vitale, A. P. Lundgren, M. Evans, K. Kawabe, S. E. Dwyer, K. Izumi, R. M. S. Schofield, A. Effler, D. Sigg, P. Fritschel, M. Drago, *et al.*, Phys. Rev. D **99**, 042001 (2019), arXiv:1806.00532 [astro-ph.IM].
- [27] P. Jung, S. H. Oh, Y.-M. Kim, E. J. Son, T. Yokozawa, T. Washimi, and J. J. Oh, Phys. Rev. D **106**, 042010 (2022).
- [28] A. Marin, D. Shoemaker, and R. Weiss, “Subtracting narrow-band noise from ligo strain data in the third observing run,” LIGO Technical Report LIGO-T970127-02-D.
- [29] E. Cuoco, J. Powell, M. Cavaglià, K. Ackley, M. Bejger, C. Chatterjee, M. Coughlin, S. Coughlin, P. Easter, R. Essick, H. Gabbard, T. Gebhard, S. Ghosh, L. Haegel, A. Iess, D. Keitel, Z. Marka, S. Marka, F. Morawski, T. Nguyen, R. Ormiston, M. Puerrer, M. Razzano, K. Staats, G. Vajente, and D. Williams, arXiv e-prints , arXiv:2005.03745 (2020), arXiv:2005.03745 [astro-ph.HE].
- [30] G. Vajente, Y. Huang, M. Isi, J. C. Driggers, J. S. Kissel, M. J. Szczepańczyk, and S. Vitale, Phys. Rev. D **101**, 042003 (2020), arXiv:1911.09083 [gr-qc].
- [31] R. Ormiston, T. Nguyen, M. Coughlin, R. X. Adhikari, and E. Katsavounidis, arXiv e-prints , arXiv:2005.06534 (2020), arXiv:2005.06534 [astro-ph.IM].
- [32] T. S. Yamamoto, S. Kuroyanagi, and G.-C. Liu, Phys. Rev. D **107**, 044032 (2023).
- [33] S. J. Zhu, M. A. Papa, and S. Walsh, Phys. Rev. D **96**, 124007 (2017), arXiv:1707.05268 [gr-qc].
- [34] D. Jones, L. Sun, J. Carlin, L. Dunn, M. Millhouse, H. Middleton, P. Meyers, P. Clearwater, D. Beniwal, L. Strang, A. Vargas, and A. Melatos, Phys. Rev. D **106**, 123011 (2022).
- [35] S. Suvorova, L. Sun, A. Melatos, W. Moran, and R. J. Evans, Phys. Rev. D **93**, 123009 (2016), arXiv:1606.02412 [astro-ph.IM].
- [36] The LIGO Scientific Collaboration, the Virgo Collaboration, the KAGRA Collaboration, R. Abbott, T. D. Abbott, F. Acernese, K. Ackley, C. Adams, N. Adhikari, R. X. Adhikari, *et al.*, arXiv e-prints , arXiv:2111.03606 (2021), arXiv:2111.03606 [gr-qc].
- [37] “Gravitational Wave Open Science Center,” <https://www.gw-openscience.org/>.
- [38] P. Jaranowski, A. Królak, and B. F. Schutz, Phys. Rev. D **58**, 063001 (1998), arXiv:gr-qc/9804014 [gr-qc].
- [39] D. M. Macleod, J. S. Areeda, S. B. Coughlin, T. J. Massinger, and A. L. Urban, SoftwareX **13**, 100657 (2021).
- [40] B. Widrow, J. Glover, J. McCool, J. Kaunitz, C. Williams, R. Hearn, J. Zeidler, J. Eugene Dong, and R. Goodlin, Proceedings of the IEEE **63**, 1692 (1975).
- [41] S. Haykin, *Adaptive Filter Theory*, 4th ed. (Prentice Hall, Upper Saddle River, New Jersey, 07458, 2002).
- [42] A. Viterbi, IEEE Transactions on Information Theory **13**, 260 (1967).
- [43] B. G. Quinn and E. J. Hannan, *The Estimation and Tracking of Frequency*, Cambridge Series in Statistical and Probabilistic Mathematics (Cambridge University Press, 2001).
- [44] J. Cheer, V. Patel, and S. Fontana, The Journal of the Acoustical Society of America **145**, 3095 (2019), https://pubs.aip.org/asa/jasa/article-pdf/145/5/3095/15336560/3095_1_online.pdf.
- [45] S. M. Kuo and J. Kunduru, Journal of the Franklin Institute **333**, 669 (1996).
- [46] K. Kokkinakis, B. Azimi, Y. Hu, and D. R. Friedland, Trends in Amplification **16**, 102 (2012), pMID: 22923425, <https://doi.org/10.1177/1084713812456906>.
- [47] S. S. Chowdhury, R. Hyder, M. S. B. Hafiz, and M. A. Haque, IEEE Journal of Biomedical and Health Informatics **22**, 450 (2018).
- [48] Y. Gong and C. Cowan, in *2004 IEEE International Conference on Acoustics, Speech, and Signal Processing*, Vol. 2 (2004) pp. ii–825.
- [49] A. Kar and M. Swamy, Signal Processing **131**, 422 (2017).
- [50] A. Kar, A. Anand, and M. Swamy, Applied Acoustics **158**, 107043 (2020).

ACKNOWLEDGMENTS

This research has made use of data, software and/or web tools obtained from the Gravitational Wave Open Science Center (<https://www.gw-openscience.org>), a service of LIGO Laboratory, the LIGO Scientific Collaboration and the Virgo Collaboration. LIGO is funded by the U.S. National Science Foundation. Virgo is funded by the French Centre National de Recherche Scientifique (CNRS), the Italian Istituto Nazionale della Fisica Nucleare (INFN) and the Dutch Nikhef, with contributions by Polish and Hungarian institutes.